ADVANCED OPTICAL MATERIALS
www.advopticalmat.de

Antimony-Rich $GaAs_xSb_{1-x}$ Nanowires Passivated by Organic Sulfides for High-Performance Transistors and Near-Infrared Photodetectors

*Wei Wang, SenPo Yip, You Meng, Weijun Wang, Fei Wang, Xiuming Bu, Zhengxun Lai, Xiaolin Kang, Pengshan Xie, Quan Quan, Chuntai Liu, and Johnny C. Ho**

Due to their excellent properties, ternary $GaAs_xSb_{1-x}$ nanowires have been extensively investigated to enable various nanodevice structures. However, the surfactant effect of antimony has a notorious impact on the surface morphology and electrical properties of prepared Sb-rich nanowires, restricting their practical utilization. Herein, through the in situ passivation effect of thiourea, highly-crystalline, uniform, and thin $GaAs_xSb_{1-x}$ nanowires ($x \leq 0.34$) are successfully achieved. In contrast to low-melting-point sulfur powders typically used in surfactant-assisted chemical vapor deposition, thiourea has a relatively higher melting point, facilitating the more controllable formation of Sb_xS_y layer on the nanowire surface to minimize the radial growth and to stabilize the sidewalls for high-quality Sb-rich nanowires. When configured into field-effect transistors, the obtained GaSb nanowires exhibit excellent device performance with a hole mobility of over 200 $cm^2 V^{-1} s^{-1}$. The optimal $GaAs_{0.18}Sb_{0.82}$ device yields an impressive responsivity of 5.4×10^4 A W^{-1} and an external quantum efficiency of 4.4×10^6% under near-infrared light illumination. Importantly, the rise and decay times are as efficient as 80 and 104 µs, respectively, which are better than any values reported for GaAsSb nanowire photoconductors to date. All these results demonstrate the promising potential of $GaAs_xSb_{1-x}$ nanowires for high-mobility electronics and ultrafast near-infrared optoelectronics.

1. Introduction

In the past decades, due to the extraordinary and versatile properties such as appropriate direct bandgap, inherent high carrier mobility, and substantial light-to-current conversion efficiency, 1D III–V semiconductor nanowires (NWs) have attracted considerable attention as building blocks for future applications in electronics and optoelectronics.[1] As compared to their bulk material counterparts, the reduced dimensionality of III-V NWs would provide them the superior surface-to-volume ratio, wave-guiding properties, light polarization sensitivity, and efficient strain relaxation to reduce lattice defects for enhanced crystallinity for technological utilization.[1d,2] In particular, the ternary NW materials systems, including InGaAs, InGaSb, and GaAsSb, have additional degrees of freedom in lattice engineering and bandgap manipulation, making them the promising active elements for a variety of field-effect transistors (FETs) and broadband photodetectors.[3] For example, GaAsSb NWs are one of the ideal active photosensing materials in the infrared optical communication region. They are also advantageous to form various band alignments (i.e., type I, II or III) with other III-V compounds.[2b,4]

However, although there is a significant recent advance in the material synthesis, it is still a challenge to achieve high density and crystalline GaAsSb NWs, especially with high Sb composition in a controllable manner. In this case, various synthesis methods have been explored to fabricate the high-quality ternary GaAsSb NWs, mainly on the basis of vapor–liquid–solid (VLS) growth mechanism. Recently, Li et al. reported the Ga self-catalyzed growth of GaAsSb NWs with pure zinc-blende (ZB) crystal structure by molecular-beam epitaxy (MBE). When configured in back-gated FETs, these NWs exhibited the clear *p-type* characteristics.[3e] In addition, the gold-seeded GaAsSb NWs with Sb content of below 60 at% were also realized by metalorganic vapor phase epitaxy, while the impact of feeding flow rate of the Sb precursor of trimethylantimony on the NW morphology and crystal structure was delicately investigated.[5] Similarly, a two-step growth method was employed to assist in

W. Wang, Y. Meng, W. J. Wang, F. Wang, X. Bu, Z. Lai, X. Kang, P. Xie, Q. Quan, J. C. Ho
Department of Materials Science and Engineering
City University of Hong Kong
Kowloon, Hong Kong SAR 999077, China
E-mail: johnnyho@cityu.edu.hk

S. P. Yip, J. C. Ho
Institute for Materials Chemistry and Engineering
Kyushu University
Fukuoka 816-8580, Japan

Y. Meng, F. Wang, J. C. Ho
State Key Laboratory of Terahertz and Millimeter Waves
City University of Hong Kong
Kowloon, Hong Kong SAR 999077, China

C. Liu
Key Laboratory of Advanced Materials Processing & Mold (Zhengzhou University)
Ministry of Education
Zhengzhou 450002, China

The ORCID identification number(s) for the author(s) of this article can be found under https://doi.org/10.1002/adom.202101289.

DOI: 10.1002/adom.202101289

obtaining high-density GaAsSb NWs with Sb composition up to 34 at% by MBE.[6] In any case, the Sb composition beyond 30 at% in the GaAsSb NW system tends to have a detrimental influence on NW surface and physical properties, inducing the formation of tapered and kinked morphology, multiple facets and thick parasitic islands growth.[7] Prepared by the aforementioned methods, the obtained GaAsSb NWs with Sb composition of over 60% are usually very thick (i.e., more than 200 nm), and the axial length is even below 2 μm, even though the growth parameters had been subtly adjusted within a narrow process window. In this regard, these NWs are not favorable for the fabrication of nanoscale electronic and optoelectronic devices because of the short channel effects and associated ineffective gate electrostatic control caused by the small aspect ratio.[1c,8]

In general, the substantially high Sb precursor concentration is required to achieve the rich Sb composition in GaAsSb NWs. Simultaneously, due to the surfactant effect, Sb is prone to float on the top of the growing surface of Sb-based NWs during synthesis, impeding the Ga side-facet diffusion and leading to the decreased axial growth rate.[7a,9] Meanwhile, the concomitant radial growth on the sidewalls via vapor-solid (VS) mechanism would give rise to the tapered morphology and parasitic islands on surface, which pronouncedly deteriorates the electronic transport properties of NWs.[7b,10] In order to tackle all these issues, herein, we employ a kind of organic sulfides (i.e., thiourea, $SC(NH_2)_2$) for the first time to suppress the unintentional radial growth to obtain thin and uniform GaSb and GaAsSb NWs via the solid-source chemical vapor deposition (SS-CVD) process. Similar to other sulfide solutions, when thiourea is heated to 180 °C or above, hydrogen sulfide (H_2S) gas would be gradually released.[11] These H_2S species are commonly utilized for the surface passivation of III-V semiconductor by forming III−S and V−S bonds.[12] In contrast to the sulfur powders exploited in our previous GaSb NW works,[13] the relatively higher melting point of thiourea makes it to evaporate more controllably in the CVD chamber, inducing more uniform NW growth with less agglomeration and widening the growth process window. In this way, crystalline and stoichiometric $GaAs_xSb_{1-x}$ NWs ($x \leq 0.34$) with smooth surface and thin, uniform diameter (less than 30 nm) without any tapering can be readily achieved. By systematically varying the As and Sb concentrations, the effect of chemical composition on their electrical and optoelectronic properties of $GaAs_xSb_{1-x}$ NWs can be explicitly investigated when they are configured into NW FET devices, where these valuable findings are scarcely reported in the literature due to the limited synthesis of high-quality GaAsSb NWs. Interestingly, it is revealed that the hole mobility of GaAsSb NWs witness an upward trend with the increasing Sb composition, reaching a maximum (≈200 $cm^2\ V^{-1}\ s^{-1}$) for GaSb NWs with a high I_{ON}/I_{OFF} ratio of $>10^3$. For near-infrared (NIR) photodetection, the $GaAs_{0.18}Sb_{0.82}$ NW devices deliver a respectable performance at room temperature with a responsivity of 5.4×10^4 A W^{-1}, a specific detectivity of 2.5×10^{10} Jones and an external quantum efficiency (EQE) of 4.4×10^6%, and a response time of 80 μs under 1550 nm illumination at a bias voltage of 2 V. This efficient response in the tens of microsecond range is one of the fastest among all the NW NIR photodetector reported so far. These excellent device performances can evidently demonstrate the great potential of ternary $GaAs_xSb_{1-x}$ NWs for future electronic and optoelectronic applications.

2. Results and Discussion

As depicted in the schematic illustration in **Figure 1**a, thiourea is utilized as surfactant for the Au-catalyzed SS-CVD growth of GaSb and GaAsSb NWs. During the growth, 1 g of thiourea powder is placed in an Al_2O_3 crucible positioned in the location between the source and the substrate heating zones, where the H_2S species is controllably released to the downstream for the formation of Ga−S and Sb−S bonds on the NW growth surface. This surface passivation is an effective way to stabilize the high-energy growth front of Sb-based III-V NWs in order to suppress their uncontrolled radial growth.[7a,14] More importantly, this passivation scheme does not induce any adverse effect on the manipulation of the chemical composition of $GaAs_xSb_{1-x}$ NWs by simply varying the precursor powder mixing ratio (i.e., the amount of GaAs and GaSb powders). The detailed NW growth and passivation mechanism will be discussed in the section later.

For a consistent comparison, pristine GaSb and GaAsSb NWs have also been grown with the same process condition without using any thiourea surfactant. In specific, Figure 1b shows the relatively thick pristine GaSb NWs obtained with the obviously kinked morphology and parasitic islands growth. Based on the corresponding transmission electron microscopy (TEM) image as presented in Figure 1d, there are spherical catalytic seeds clearly observed at the NW tips, indicating that the NW growth follows the VLS mechanism. It is also noted that there is a significant tapering behavior, mainly attributable to the excessive NW radial growth. Except for the direct impingement upon Au catalyst droplets from the Ga precursor, the catalytic droplets also collect the Ga atoms via the Ga adatom diffusion toward the NW tip-body interface, which originates from the adsorption of the substrate surface and the NW side facets.[15] However, the Sb atoms would react with the Ga atoms adsorbed on the NW side-facet surfaces and reduce the diffusion length of Ga adatoms on the facets, leading to the enhancement of the radial growth and the tapered morphology via VS mechanism. By contrast, the utilization of thiourea would dramatically improve the surface morphology by minimizing the kinked morphology, reducing the diameters, and increasing the growth density of GaSb NWs as witnessed in the scanning electron microscope (SEM) image in Figure 1c. Evidently, the smaller diameters of the thiourea-assisted GaSb NWs are found to be uniformly distributed along the axial direction, strikingly demonstrating the effective suppression of the uncontrolled radial NW growth (Figure 1e). From the statistics of more than 70 NWs for each sample group, the average diameter of thiourea-assisted GaSb NWs is 36 ± 5 nm, which is much smaller as compared to those (166 ± 50 nm) of growing without any thiourea surfactant (Figure 1f). To further evaluate the crystallinity and the growth orientation of thiourea-assisted GaSb NWs, high-resolution transmission electron microscopy (HRTEM) was carried out as displayed in Figure 1g. An amorphous native oxide shell is observed with a thickness of about 3 nm. The

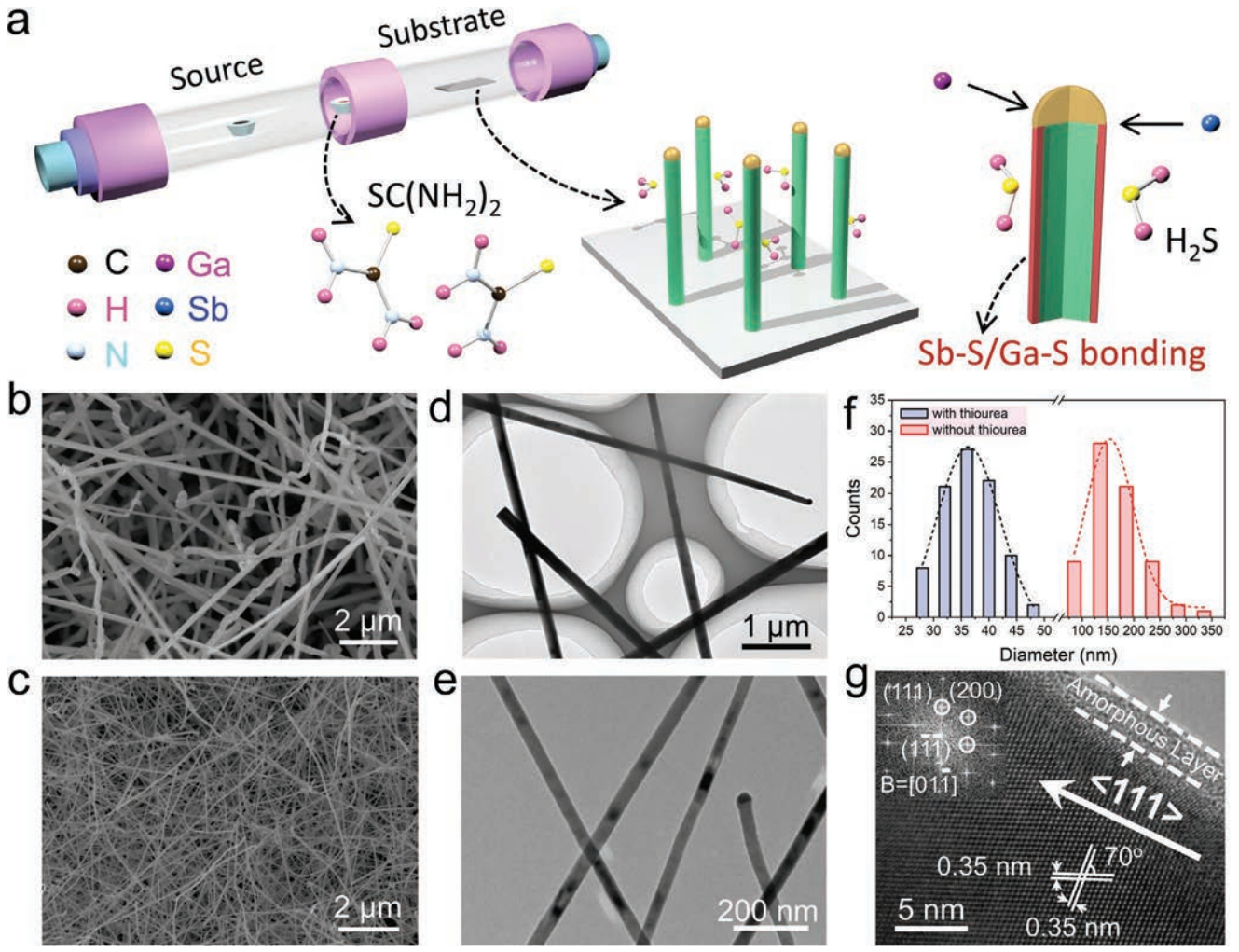

Figure 1. a) Schematic illustration of the synthesis process of GaSb NWs with thiourea as surfactant. b,c) SEM images of GaSb NWs grown without and with thiourea, respectively. d,e) TEM images of GaSb NWs without and with thiourea, accordingly. f) Statistics of the diameter distribution of the obtained GaSb NWs. g) HRTEM image of the thiourea-assisted grown GaSb NW body. The inset shows the fast Fourier transform pattern of the NW body.

figure inset shows the corresponding fast Fourier transform (FFT) pattern of the NW, illustrating the single crystalline zinc blende structure and its preferential <111> growth orientation. This direction is typically observed in III-V semiconductor NW growth since it consists of the lowest free surface energy planes for the NW nucleation and formation.[16] In addition, there is not any significant amount of crystal defects, such as stacking faults or twin-plane polytypic defects, were identified in the NW sample, which suggests the excellent crystal quality and the good control of the thiourea-assisted growth process of GaSb NWs. The crystal structure of pristine GaSb NWs without any thiourea passivation is also assessed and confirmed to be crystalline in the zinc blende structure (Figure S1, Supporting Information). As a result, the introduction of thiourea does not influence the crystal structure of the obtained NWs, while it suppresses the notorious uncontrolled radial growth to achieve the thin, long, and uniform NWs here.

In the meanwhile, it is necessary to explicitly reveal the role of thiourea in the NW synthesis. As a type of organic sulfide, thiourea is usually utilized to serve as the sulfur source for target applications.[17] Once thiourea is heated to above 180 °C, the gaseous products, mainly comprising of H_2S and NH_3, would be controllably released,[11a,b] in which H_2S is frequently employed to surface-passivate the III-V semiconductors by forming the III−S and V−S bonds on the surface. For instance, Fukuda et al. reported that the H_2S-treatment could effectively reduce the unoccupied surface states of GaP due to the passivation of dangling bonds.[12a,b] Therefore, X-ray photoelectron spectroscopy (XPS) measurements were performed in this work to assess the NW constituents' chemical state. Prior to the XPS measurements of GaSb NWs, in order to confirm whether the sulfur atoms are indeed incorporated into the NW core or only bond to the surface, the outer shells of NWs were first removed by etching them in the dilute HF solution (1 vol%) for 1 min and immediately followed by the deionized water rinse. It is worth mentioning that the surface morphology of processed GaSb NWs did not get damaged as the NWs were still long and dense with smooth surfaces after etching (**Figure 2**a; and Figure S2a, Supporting Information). The average NW diameter is then shrunk from initial 36 nm down to 30 nm after the HF

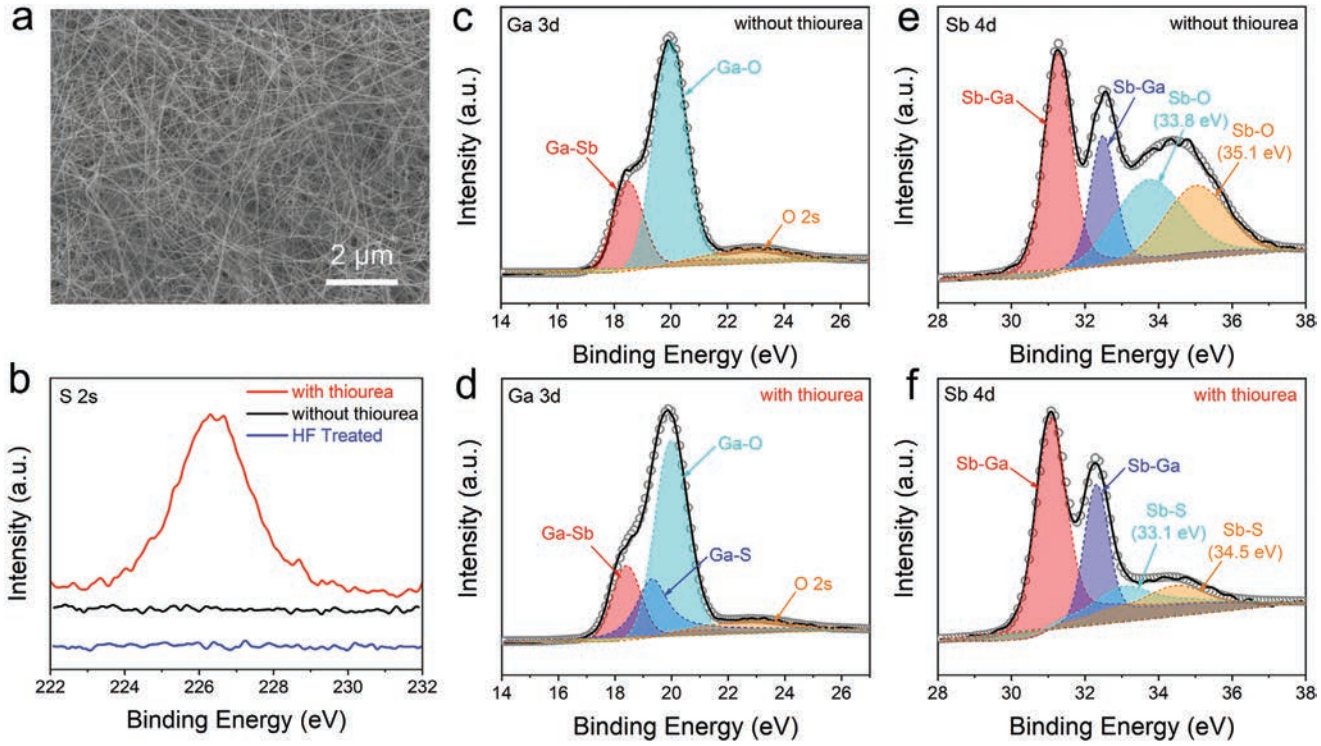

Figure 2. a) Surface morphologies of the thiourea-assisted grown GaSb NWs processed with 1 vol% HF solution for 1 min. XPS studies of the GaSb NWs grown with or without thiourea and those processed with HF: b) S 2s spectra; c,d) deconvoluted Ga 3d profiles of GaSb NWs without and with thiourea, respectively; e,f) deconvoluted Sb 4d profiles of GaSb NWs without and with thiourea, accordingly.

treatment (Figure S2b, Supporting Information), indicating the outmost amorphous shell (≈3 nm as shown in Figure 1g) could be completely removed by this ex situ treatment. In this case, XPS analysis was subsequently carried out by focusing on the core levels of the spectra of S 2s, Ga 3d, and Sb 4d for the three different sample groups, i.e., GaSb NWs grown with/without thiourea and the HF-treated NWs with thiourea passivation. All the XPS spectra have been calibrated with the reference peak of C 1s (284.6 eV). As shown in the S 2s spectra in Figure 2b, the S core level is only observed in the thiourea-passivated sample without HF etching, ascertaining that the S atoms only exist on the NW surface and the possibility of incorporating the S atoms into the NW core by surface passivation could be ruled out. Moreover, it is clear that the spectrum of Ga 3d without any sulfide modification can be decomposed into three components by Gauss–Lorentz fitting, corresponding to the Ga—Sb (at 18.5 eV), Ga—O (at 20.0 eV), and O 2s (at 23.1 eV) bonds, respectively (Figure 2c). For the sulfide passivated sample, a new component arises in the oxide component area of Ga 3d, with the binding energy shift to a lower value with respect to Ga—O by –0.7 eV, which could be assigned to the Ga—S bonding (Figure 2d).[18] Interestingly, the Ga—O peaks are more intense than other Ga 3d peaks (e.g., Ga—Sb peaks) for both NW samples with or without thiourea passivation; therefore, the Ga atoms on the NW surface are prone to be oxidized when exposed to the ambient, also elucidating the minor effect of thiourea on Ga atoms due to the relatively weak Ga—S bonding. This way, it makes sense that the intensity of Ga—O peak gets apparently diminished after HF etching (Figure S2c, Supporting Information). At the same time, based on the peak fitting of the Sb 4d spectrum, the chemical bonds of Ga—Sb ($4d_{5/2}$ at 31.3 eV and $4d_{3/2}$ at 32.5 eV) and Ga—O ($4d_{5/2}$ at 33.8 eV and $4d_{3/2}$ at 35.1 eV) are observed for the pristine unprocessed NWs (Figure 2e). In contrast, there is a significant reduction in the relative magnitude of the oxide component area of Sb 4d core levels for the thiourea-processed samples (Figure 2f). These two components' binding energies are also observed to shift to 33.1 and 34.5 eV, respectively, which can be designated to the formation of Sb—S bonds.[19] Therefore, these peak intensity differences and binding energy shifts between the samples with and without thiourea treatment can confirm a noticeable effect of thiourea on the passivation of GaSb NWs. The Sb—S bonds are established on the NW surface to inhibit the surfactant effect of Sb and thus stabilize the NW sidewalls. After HF treatment, the Sb—O bonds are witnessed to emerge with relatively high intensity (Figure S2d, Supporting Information). This is mainly caused by the exposure of adjacently inner Sb atoms to the ambient that results from the removal of outmost amorphous shells, convincingly proving the passivation mechanism of thiourea by forming Sb—S bonding on the NW side-facet surface.

Besides H_2S, it is also important to investigate the impact of another gaseous product, NH_3, on the surface morphology and chemical composition of GaSb NWs. In this case, the growth of GaSb NWs under the condition of NH_3 gas flow without using any thiourea was purposely implemented. As depicted in Figure S3a,b (Supporting Information), there are substantial surface coating and kinked morphology observed for the large-diameter NWs, similar to the pristine NWs grown

without any surfactant, which manifests that the introduction of NH_3 can hardly surface-passivate the GaSb NWs. Due to the severe inference of N 1s binding energy with the strong Ga Auger peak in XPS measurements, electron energy loss spectroscopy (EELS), instead of XPS, was employed to characterize the elemental composition of the obtained NH_3-enabled NWs. It is clear that there is homogeneous distribution of Ga and Sb along the NW body, whereas the scarce presence of N indicates the absence of N adsorption or passivation on the NW surface (Figure S3c,d, Supporting Information). All these findings have further confirmed that the thinning of GaSb NWs could be dominantly ascribed to the existence of H_2S. Without using any surfactant, the GaSb NW would be grown with abundant surface Ga_xO_y and Sb_xO_y layers as evidenced in the XPS spectra discussed before. When the thiourea is utilized, the GaSb NW sidewall would be stabilized by the formation of Sb_xS_y layer (coexisting with Ga_xS_y and Ga_xO_y). As a result, the electrical device properties of surface-passivated NWs are anticipated to be correspondingly enhanced for the reduced surface states and the reinforced gate electrostatic control.

To evaluate the electrical properties of prepared GaSb NWs, global back-gated NW FETs were fabricated with individual GaSb NWs as device channels by using Ni source/drain electrodes (≈60 nm) with the same configuration as previously reported.[3a] As given in the transfer characteristics in **Figure 3**a,b, both the NW devices with and without thiourea treatment deliver a typical intrinsic *p-type* semiconducting behavior. It is worth noting that the thiourea-passivated GaSb NW device has remarkably enhanced the FET device properties, exhibiting a large on-state current (480 nA), a low off-state current (36 pA), and an impressively high on/off current ratio (>10^4) under V_{ds} = 0.1 V as compared with the counterpart without thiourea treatment. The output characteristics of the device configured with the thiourea-treated NW channel are displayed in Figure 3c, where the linear relationship demonstrates the ohmic-like contact behavior between Ni electrodes and NW channels. Meanwhile, the field-effect hole mobility (μ) can be extracted and calculated from the transfer characteristics by the following analytic expression[20]

$$\mu = g_m \cdot \frac{L^2}{C_{OX}} \cdot \frac{1}{V_{ds}} \tag{1}$$

where g_m is the transconductance defined as dI_{ds}/dV_{gs}, L is the NW channel length, C_{OX} is the gate oxide capacitance, and V_{ds} is the source–drain bias. C_{OX} can be derived from the finite element method by using COMSOL software.[3c] Then, the peak mobility of the thiourea-passivated NW device is calculated to be as high as ≈200 $cm^2\ V^{-1}\ s^{-1}$, which almost quadruples the value of the thick GaSb NW device without thiourea treatment (Figure 3d). Statistical results of the peak mobility and on/off current ratio values of the devices are also compiled in Figure 3e,f, further proving the significant improvement of FET properties after the passivation treatment of thiourea. The variations of mobility and on/off current ratio for each sample group can be attributed to the different NW diameter, surface roughness, crystallinity, and other factors that can affect the NW FETs' electrical properties.

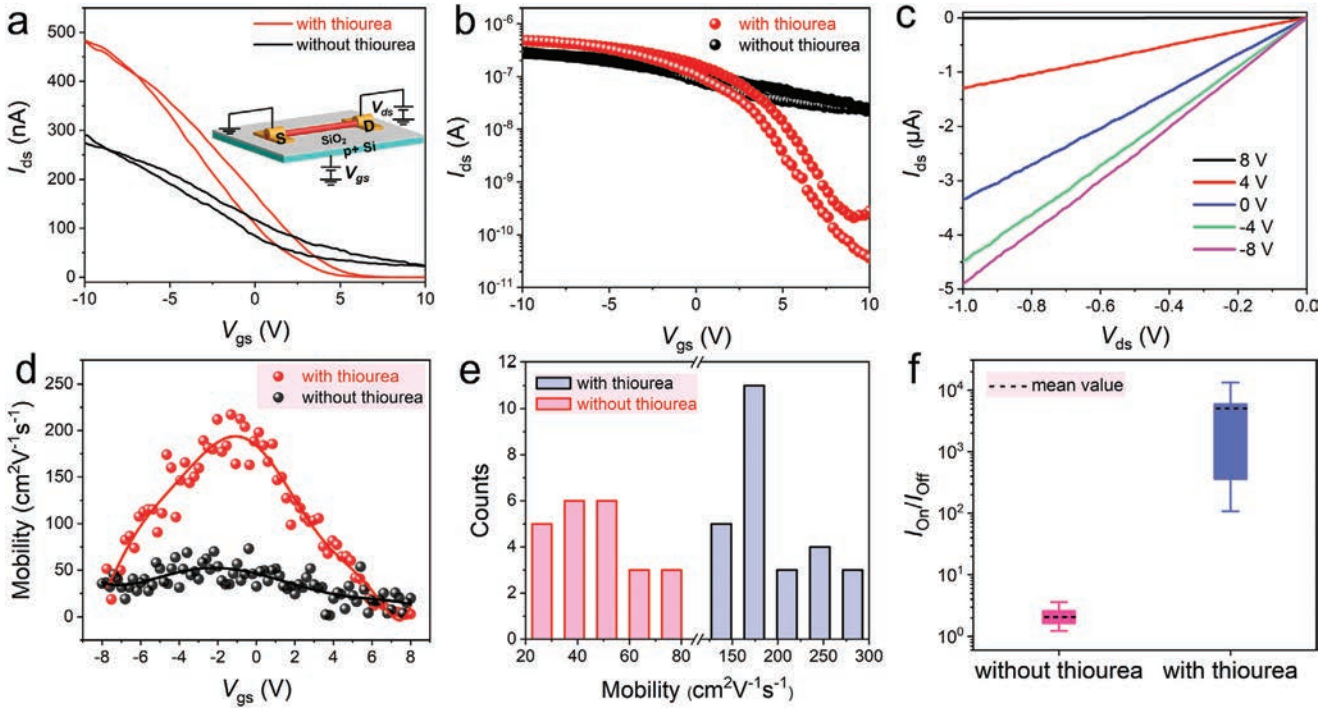

Figure 3. a,b) Transfer characteristics of the NW FET configured by using a single thiourea-treated and -untreated GaSb NW channel under source–drain bias of 0.1 V, respectively. The schematic diagram of the device configuration is shown in the inset. c) Output characteristics of the NW FET configured by using a single thiourea-treated GaSb NW channel. d) Mobility of the corresponding devices presented in panel a). e,f) Statistics of the mobility distribution and on-off current ratio of thiourea-treated and untreated GaSb NW FETs.

In general, the device performance enhancement is mainly due to the better NW crystallinity and the much larger aspect ratio for more efficient gate coupling resulted from the surfactant passivation. Based on the forward I_{ds}–V_{gs} sweep of the transfer characteristics presented in Figure 3a, the free hole carrier concentration can be estimated by the analytical equation[21]

$$n_h = \left| \frac{4C_{OX}\left(V_{gs} - V_{th}\right)}{\pi q d^2 L} \right| \quad (2)$$

where V_{th} is the device threshold voltage, d and L are the diameter and length of the NW channel, respectively. As compared with the FET device based on the thiourea-passivated NW channel, the thicker NW FET exhibits a lower carrier concentration at the zero gate voltage and the n_h value decreases from 2.88×10^{17} to 1.37×10^{17} cm^{-3}, accordingly. On the one hand, with thiourea treatment, the GaSb NW surface states would be passivated and thus fewer carriers could be trapped by the NW surface. In this way, the improved NW crystallinity with minimal crystal defects is beneficial to augmenting free carrier concentration. In addition, the diameter of thiourea-treated GaSb NWs is substantially reduced as compared to those untreated NWs. This aggressive NW diameter scaling would offer better gate electrostatic control, which yields the lower drive voltages while maintaining sufficient on-sate current and lowering off-state current for the minimized power consumption as explicitly evidenced in Figure 3e,f.[8,22] It is also noted that although the NW diameter can be shrunk by HF etching, this surface etching is not an ideal approach to achieve thin NWs due to the significant amount of trap states induced, deteriorating the electrical properties of NW devices (Figure S2e,f, Supporting Information). In any case, the NW growth with thiourea contributes to the larger aspect ratio of the GaSb NWs and the improved crystal quality for the remarkable enhancement of NW FET device performance.

Apart from GaSb NWs, thiourea is also found to play an effective role in improving the surface quality and controlling the diameter of ternary Sb-rich $GaAs_xSb_{1-x}$ NWs (with precursor powder mixing ratio of GaSb:GaAs = 20:1 in wt%). The ternary NWs are also grown without using any surfactant with the same growth condition for a consistent comparison. At first, the NW morphologies were evaluated by employing SEM and TEM. Based on the SEM and TEM images displayed in **Figure 4**a,c, the $GaAs_xSb_{1-x}$ NWs without any passivation exhibit the poor morphology with significant tapering, which presents a similar feature with the unmodified GaSb NWs on account of high Sb concentration. By contrast, the participation of thiourea in the growth can noticeably eliminate the kinked and tapering behaviors, thus achieving the far thinner NWs as shown in Figure 4b,d. The diameter distribution was assessed from the TEM images and illustrated in Figure 4e. It is evident that the passivated NWs are relatively thin with a narrow diameter distribution (29 ± 4 nm) as compared to the thiourea-untreated ones (190 ± 43 nm). Notably, the NW sidewall roughness is identified as one of the key factors to enable impressive device performance. As demonstrated in the AFM tomography images in Figure S4a,b (Supporting Information), the GaAsSb NW grown without thiourea would have distinct parasitic growth along the axial direction, whereas dramatic changes occurred for the thiourea-assisted grown NW, having the much smoother surface without any obvious particle coatings. Therefore, thiourea can not only restrain the uncontrolled radial NW growth but also stabilize the side-facet surface of GaAsSb NWs to a great extent.

At the same time, HRTEM studies were also carried out to assess the crystallinity of as-prepared ternary GaAsSb NWs. Figure 4f and Figure S4c,d (Supporting Information) give the HRTEM images of representative GaAsSb NWs grown with and without thiourea, accordingly. The almost defect-free and highly-crystalline zinc blende phase is confirmed for both NW samples. The FFT patterns demonstrate the growth orientation along <111> and <110> direction, respectively, both of which are very common in III-V NW growth. Their chemical composition could be determined by using energy dispersive X-ray spectroscopy (EDS), where they are found to be $GaAs_{0.05}Sb_{0.95}$ and $GaAs_{0.12}Sb_{0.88}$ for the samples with and without thiourea (Figure S5, Supporting Information). The relatively significant difference in As concentration could be attributed to the reservoir effect in ternary III-V semiconductor NWs that has been reported previously.[4a,23] The exchange of As for Sb at the NW surface during growth would cause outward diffusion of Sb or radial GaAs overgrowth, which can be demonstrated by the apparent parasitic growth phenomenon (Figure S4a, Supporting Information). In this study, for the GaAsSb NWs, the As–Sb exchange at the NW surface during growth would result in the composition inhomogeneity and the accumulation or clusters of As atoms. However, with the sidewall stabilization by using thiourea surfactant, the diffusion of As and Sb adatoms along the NW surface is anticipated to be hindered, leading to the suspension of As–Sb exchange and parasitic growth on the NW surface. Consequently, the thin NWs with smooth surfaces together with relatively low and homogeneous As composition would then be achieved. EDS mappings were as well performed on the $GaAs_{0.05}Sb_{0.95}$ NWs, where the elements of Ga, Sb, As, and S are all distributed in a uniform manner along both axial and radial directions of the NW (Figure 4g). In addition, the evenly distributed S atoms on the NW surface further confirm the existence of the surface passivation layer. All these results suggest that the thiourea-assisted SS-CVD technique can be employed to synthesize high-quality Sb-rich $GaAs_xSb_{1-x}$ NWs with well-controlled surface morphology and good crystallinity. Moreover, the pure zinc blende crystal structure without any wurtzite phase is witnessed for all GaSb and Sb-rich $GaAs_xSb_{1-x}$ NWs as illustrated in the X-ray diffraction (XRD) patterns in Figure S5c (Supporting Information), consistent with the HRTEM results as discussed above. Expectedly, the main peaks of GaAsSb NWs are found to shift toward the larger angle with the introduction of As, indicating the decreased lattice parameter due to the smaller size of As atoms replacing the Sb atoms. With comparison to the thiourea-untreated NWs, a smaller angle shift is also observed for the GaAsSb NWs with thiourea, which is in accordance with the EDS analysis that the passivation effect would limit the incorporation of As atoms into NWs through an exchange mechanism.

Subsequently, the growth of $GaAs_xSb_{1-x}$ NWs with varied chemical stoichiometry was conducted via the robust thiourea-assisted SS-CVD process. GaSb and GaAs powders in different

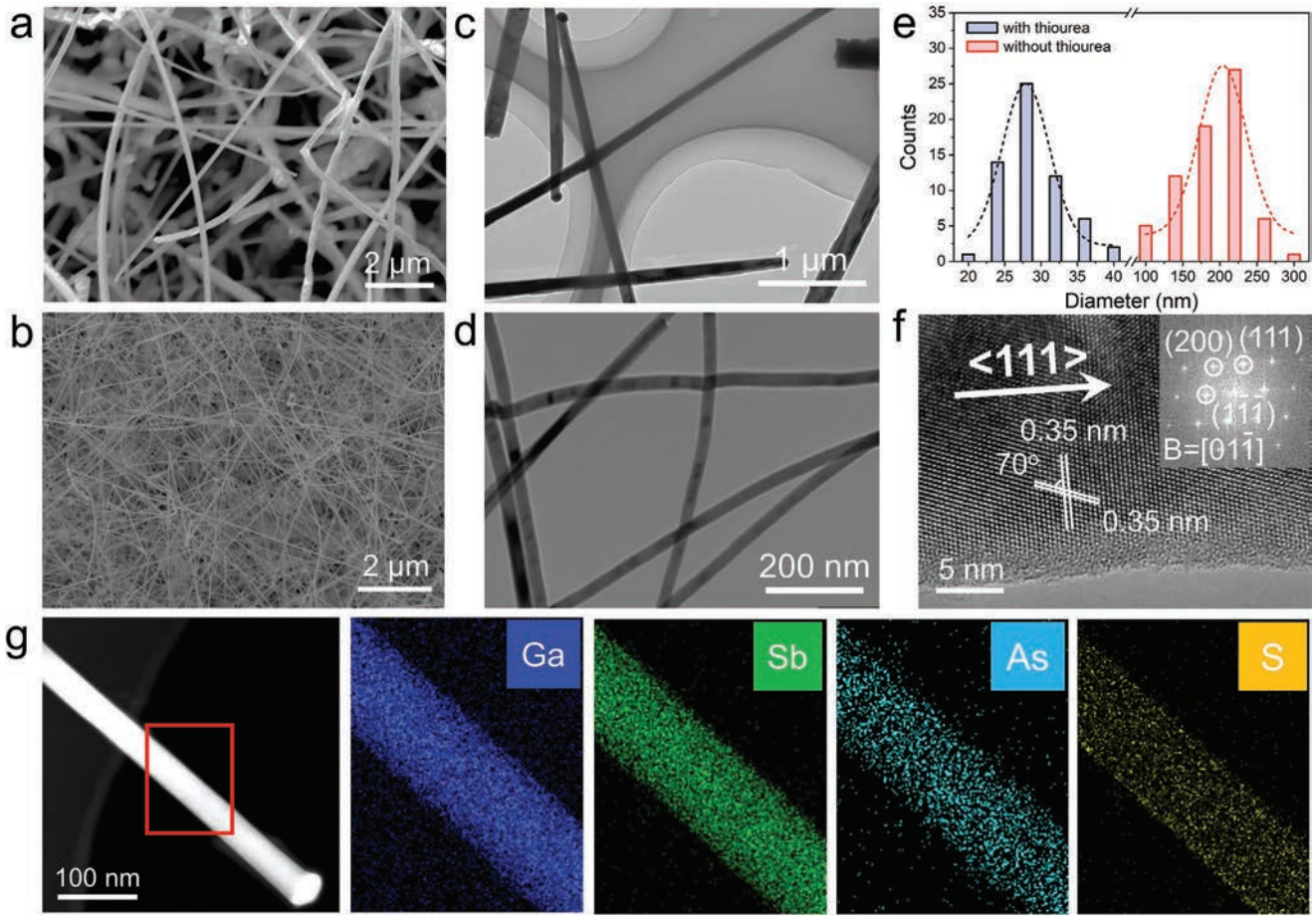

Figure 4. a,b) Surface morphologies and c,d) TEM images of GaAsSb nanowires grown without thiourea and with thiourea. e) Statistics of diameter distribution of the GaAsSb NWs grown without and with thiourea. f) HRTEM image of the thiourea-treated GaAsSb NW. The inset shows the fast Fourier transform pattern of the NW body. g) HAADAF-STEM image and corresponding EDS mapping of Ga, Sb, and As elements of the thiourea-assisted grown GaAsSb NW.

mixing ratios (i.e., 2:1, 1:1, 1:1.5, and 1:2 in wt%) were used as the precursor source. The mixed ratio can predetermine the vapor pressure of Sb and As under a specific source temperature. Therefore, it would affect the final composition of the grown ternary NWs. Here, the chemical compositions of all NWs were determined by EDS point scan based on the random statistics of more than 10 NW candidates for each sample group, where they are found to be $GaAs_{0.11}Sb_{0.89}$, $GaAs_{0.18}Sb_{0.82}$, $GaAs_{0.25}Sb_{0.75}$, and $GaAs_{0.34}Sb_{0.66}$ for the powder mixing ratio of 2:1, 1:1, 1:1.5, and 1:2 in wt%, respectively. The detailed growth parameters and NW composition are also compiled in Table S1 and Figure S6 (Supporting Information). It is evident that the lower powder mixing ratio of GaSb: GaAs would yield the $GaAs_xSb_{1-x}$ NWs with the higher As content, which is anticipated to possess different controllable electronic and optoelectronic properties. The slight variation in the chemical composition indicates the tight control over NW stoichiometry by the present CVD technique, favoring to assess the NW composition-dependent properties. Furthermore, as demonstrated in the SEM and TEM images in Figures S7 and S8 (Supporting Information), all the $GaAs_xSb_{1-x}$ NWs with the different composition are reliably achieved in high density, exhibiting the desired morphology with smooth surfaces and nontapered characteristics along the NW length, which is very beneficial to the subsequent device utilization and electronic performance enhancement. Based on the TEM characterization, the diameter measurement results of different $GaAs_xSb_{1-x}$ NWs ($0 \le x \le 0.34$) were summarized in Figure S9a–e (Supporting Information). The 95% confidence interval for the average diameter is also depicted by the error bar for each composition. As extracted from the statistics of more than 70 NWs for each sample group, the average diameter of all NWs are found to be similar, ranging from 21 to 36 nm. Obviously, there is not any significant impact made on the NW morphology and diameter variation when the As concentration is varied. Furthermore, as verified in the XRD patterns and HRTEM images (Figures S9f and S10, Supporting Information), the $GaAs_{0.11}Sb_{0.89}$, $GaAs_{0.18}Sb_{0.82}$, $GaAs_{0.25}Sb_{0.75}$, and $GaAs_{0.34}Sb_{0.66}$ NWs preserve the pure ZB crystal structure and growth direction of <111> without any obvious planar defects, although the higher As concentration is alloyed. This could be attributed to the small difference between the atomic radius of As and Sb as well as the high compatibility of As atoms with the ZB structure of GaSb. Regarding the XRD patterns, it is noteworthy that there exists a peak shift tendency toward the

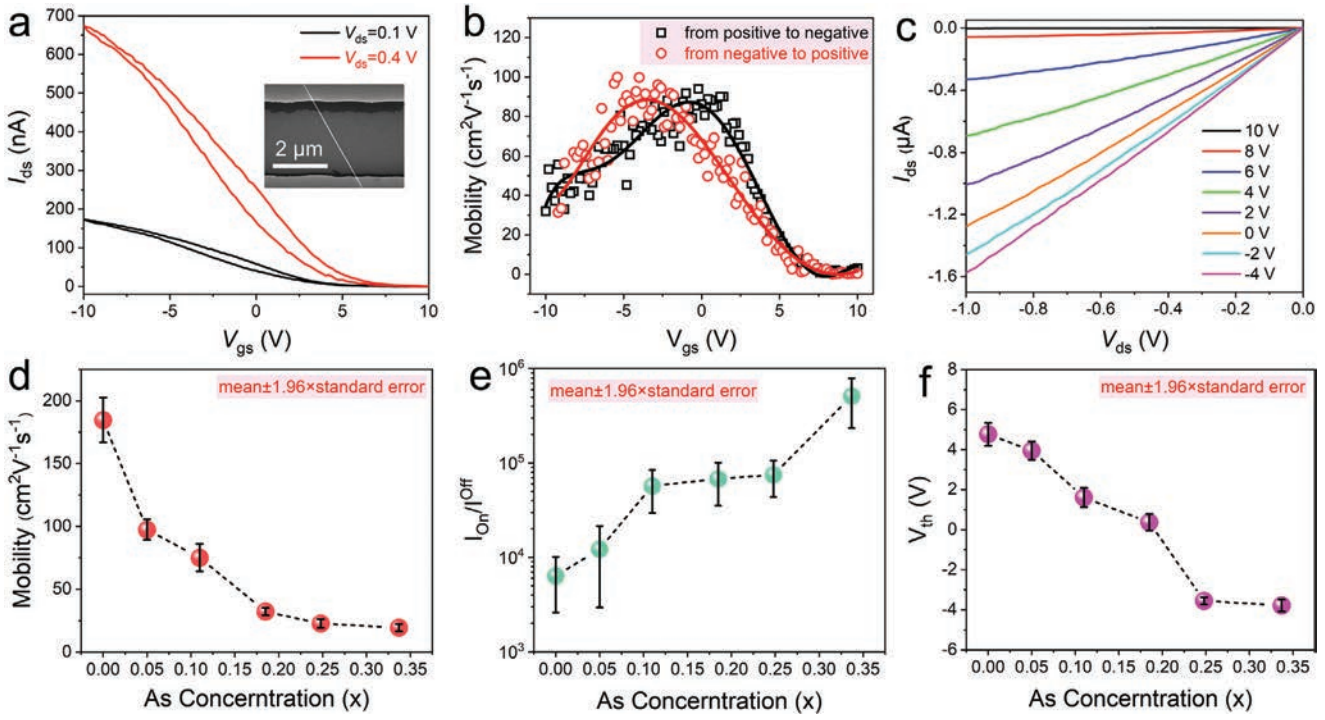

Figure 5. a) Transfer characteristics of a representative NW FET configured with a single $GaAs_{0.05}Sb_{0.95}$ NW channel. The inset shows the SEM image of the back-gated NW FET with Ni contacts. b) Mobility calculation of the NW FET presented in panel a with double-sweep measurement under source–drain bias of 0.1 V. c) Output characteristics of the NW FET device presented in panel a). d–f) Statistics of the field-effect peak hole mobility, on-off current ratio and threshold voltage as a function of As concentration. In each sample group, more than 30 different NW FET devices are evaluated.

larger 2θ value with the plots of increasing As concentration, suggesting that no phase segregation occurs. This again highlights the advantages of the thiourea-assisted CVD method for synthesizing high-quality and composition-tunable ternary GaAsSb NWs in small diameters.

Once the highly-crystalline $GaAs_xSb_{1-x}$ NWs are successfully grown by the thiourea-assisted CVD method, we can start to systematically investigate their intrinsic properties and explore their potential applications. In order to illustrate their electronic properties with varied chemical composition, the global back-gated FET devices were fabricated with Ni contacts. The device configuration is the same with that of the single GaSb NW FET in Figure 3a inset. From the typical transfer characteristics of $GaAs_{0.05}Sb_{0.95}$ NW FET, it is clear that the source–drain current (I_{ds}) decreases with the increasing gate voltage (V_{gs}), indicating the *p-type* semiconducting behavior (**Figure 5**a). As shown in the corresponding SEM image in Figure 5a inset, this NW device has a channel length of ≈3 μm. In spite of the incorporation of a certain amount of As atoms in this ternary material system, this *p-type* behavior is probably attributed to the prevalence of Sb related point defects, such as antisite defects and vacancies, acting as acceptors in the NWs.[24] The inconspicuous hysteresis in the transfer characteristics is possibly induced by the movable ions in the dielectric and absorbents from ambient, etc. Next, by applying Equation (1) based on the standard square-law model, the field-effect hole carrier mobility in the linear region can be extracted from the double-sweep I_{ds}–V_{gs} curves under source–drain bias of 0.1 V. As seen in Figure 5b, the peak hole mobility of $GaAs_{0.05}Sb_{0.95}$ NW FET is determined to be 92 cm^2 V^{-1} s^{-1}. It is also confirmed that there is a negligible error raised by the hysteresis associated with different sweep directions. More importantly, the linear relationship of I_{ds}–V_{ds} indicates the ohmic-like contact between the $GaAs_xSb_{1-x}$ NW channels and Ni electrodes (Figure 5c and Figure S11c–f, Supporting Information). To further assess the FET device properties of $GaAs_xSb_{1-x}$ NWs with different As concentration, more than 30 NW devices were measured for each As concentration, while the corresponding statistics of the extracted mobility, I_{ON}–I_{OFF} ratio and threshold voltage values are compiled in Figure 5d–f. These results show the clear stoichiometric dependence of FET device properties. With the increasing As composition, the field-effect hole mobility values witness a monoclinic decreasing trend from the average value of ≈180 to ≈20 cm^2 V^{-1} s^{-1}, whereas a contrary tendency is observed for the I_{ON}–I_{OFF} ratio. This could be related to the following three causes. First, since the *p-type* semiconducting behavior of GaAsSb NWs mainly originates from the Sb-related point defects, the hole concentration would be reduced with the increasing As content introduced into the GaSb materials, which favors to turn off the devices while deteriorates the hole mobility, leading to the dampening effect of *p-type* characteristics. As depicted intuitively in Figure S11a,b (Supporting Information), the $GaAs_{0.34}Sb_{0.66}$ NW FET exhibits the minimal on-state current and hole mobility, indicating that Sb alloying at the higher content is beneficial to the enhanced carrier concentration and the improved GaAsSb NW device performance. Second, in light of the Drude model, the charge carrier mobility (μ) is determined by the carrier effective mass

(m^*) and the momentum relaxation time (τ), with the relationship of $\mu = e\tau/m^*$.[25] Based on the Fröhlich coupling mechanism in polar inorganic semiconductors, the electron–phonon coupling would be enhanced in GaAs with respect to GaSb, which is attributed to the higher ionicity of the Ga—As bond (fractional ionic character: 0.36) as compared with that of the Ga—Sb bond (fractional ionic character: 0.26).[26] Hence, the momentum relaxation time (τ) is anticipated to decline with a higher proportion of Ga—As bonds in the ternary GaAsSb NWs. As a result, combining with the larger effective mass for the heavy and light hole bands for GaAs than GaSb, the downward trend of hole mobility would come into being with the rise of As concentration.[27] Finally, to a certain extent, GaAsSb NWs still suffer from the increased alloy scattering with the increasing As concentration despite of the similar electron affinity between As and Sb. In addition, as the As content rises, the declining trend of the threshold voltage is as well observed in Figure 5f, corresponding to the transformation from depletion mode to enhancement mode for the device operation of NW FETs. These different V_{th} values are usually associated with the various amount of carrier concentration. As explained above, the increase of As composition tends to reduce the hole concentration in the NW channel. This way, the NW FETs can be switched off more easily without applying a large positive gate voltage. From the evaluation results of the FET performance, the decrease of mobility corresponds to the reduction of V_{th} and improvement of I_{ON}–I_{OFF} ratio with the increasing As concentration in $GaAs_xSb_{1-x}$ NWs ($0 \le x \le 0.34$). These findings could provide a design guideline in choosing the appropriate chemical stoichiometry of ternary GaAsSb NWs, in which the enhancement of I_{ON}–I_{OFF} ratio and high energy-efficiency may be attained at the cost of mobility degradation. Therefore, comprehensive considerations are required to achieve the optimal device performance.

On top of the FETs, III-V semiconductors are also usually employed as superior optoelectronic materials. Nevertheless, up till now, the development of cost-effective NIR photodetectors with high stability and photosensitivity is still a challenge due to the lack of suitable active photosensing materials. Interestingly, the thiourea-assisted grown $GaAs_xSb_{1-x}$ NWs exhibited efficient photoconductive characteristics toward the shortwave infrared regime (i.e., optical communication region at 1550 nm). In specific, the FET-based photodetectors made of individual NWs were fabricated and characterized under IR illumination as shown with the device schematic in **Figure 6**a. The typical output current-voltage characteristics of $GaAs_{0.18}Sb_{0.82}$ NW photodetector were measured under various power densities (i.e., 0.019, 0.064, 0.127, 0.178, 0.271, and 0.350 mW mm^{-2}) of 1550 nm light irradiation as presented in Figure 6b. It is clear that the illuminated output current increases accordingly with the rise of light power density under a constant source–drain bias (V_{ds} = 2 V) and a zero gate bias (V_{gs} = 0 V), suggesting the effective photoresponse of the NW device. This illuminated current is generally known as the photocurrent (I_{ph}), which is defined as the current difference between the illuminated state and the dark state (i.e., $I_{ph} = I_{light} - I_{dark}$). Figure S12a (Supporting Information) shows that the as-fabricated NIR photodetector exhibits the excellent on/off switching behavior under different light intensities. To further appraise the photoresponse characteristics of the device, the dependence of measured photocurrent on varied light intensities is compiled in Figure 6c, in which the relationship can be fitted by the following power law equation

$$I_{ph} = AP^{\theta} \tag{3}$$

where A and θ are the fitting parameters and P is the light intensity. Through the fitting, the value of θ is estimated to be 0.5. Evidently, there is a sublinear upward trend in the device photocurrent with light intensity, which is typically observed for the semiconductor materials. This phenomenon primarily results from the complex electron–hole generation, trapping and recombination during the photodetection process.[28] On the other hand, photoresponsivity (R), detectivity (D^*), and external quantum efficiency (EQE) are other figure-of-merits to quantify the device performance, which can be defined as

$$R = \frac{I_{ph}}{PS} \tag{4}$$

$$D^* = R \cdot \sqrt{\frac{S}{2eI_{dark}}} \tag{5}$$

$$\mathrm{EQE} = R\frac{hc}{e\lambda} \tag{6}$$

where S is the effective irradiated area of the NW channel, e is the electronic charge, h is the Planck's constant, c is the velocity of light, and λ is the incident wavelength.[29] Here, the effective irradiated area (S) of the photodetector is calculated by the expression of $S = d \times l$ (d and l are the NW diameter and channel length, respectively). As given in Figure 6c,d, both the responsivity and detectivity are observed to increase dramatically with light intensity. Under a low light intensity of 0.015 mW mm^{-2} and a source–drain bias of 2 V, the R value is found to be as high as 5.4×10^4 A W^{-1}, while the corresponding D^* and EQE are up to 2.5×10^{10} Jones and 4.4×10^6% (Figure S12b, Supporting Information), respectively. These results illustrate the pronounced sensitivity of the NW device for NIR photodetection. Meanwhile, the photodetectors' stability and response speed are also crucial for their practical utilization. When illuminated at an intensity of 16.0 mW mm^{-2}, it is revealed that the as-fabricated NIR photodetector yields excellent periodicity and stability by periodically modulating the 1550 nm laser at a chopped frequency of 0.2 Hz (Figure 6e). The slight fluctuation of the on/off-state current could be caused by the absorption/desorption of surface molecules. It is also noted that the GaAsSb NW photodetectors show a slight persistent photocurrent when they are switched off, which can be attributed to the surface states and the Sb-related defects. The rise and decay times, defined as the time interval between 10% and 90% of the peak value of photocurrent, accordingly, can be extracted from the high-resolution photoresponse measurement (Figure 6f). The rise and decay times are determined to be 80 and 104 µs, respectively, indicating the very fast response of the device. This efficient response is one of the fastest and very competitive among all the III-V semiconductor NW NIR photodetectors reported

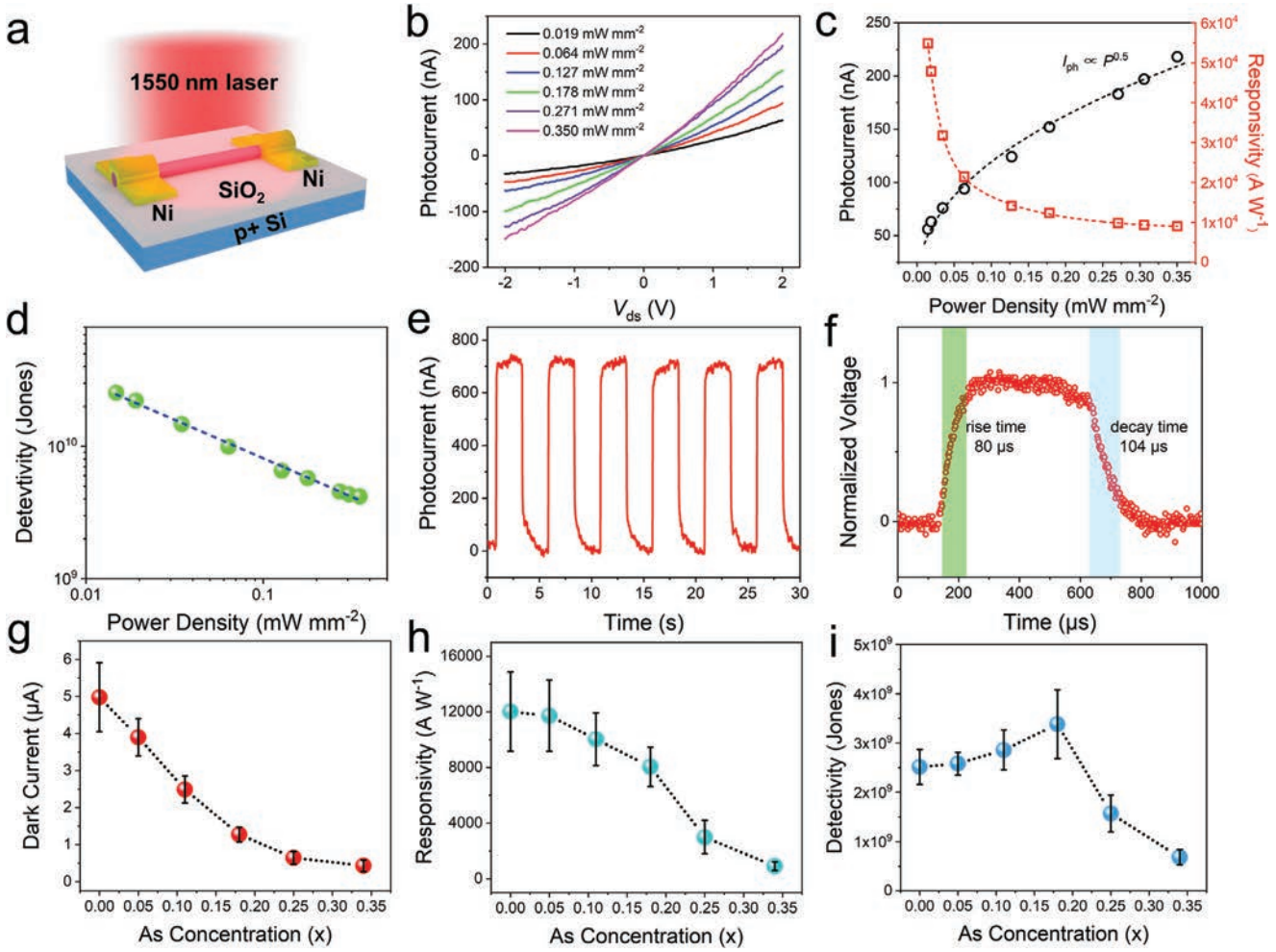

Figure 6. Infrared photodetection of single thiourea-assisted grown $GaAs_{0.18}Sb_{0.82}$ nanowire device (1550 nm laser): a) Schematic of the single NW photodetector device structure. b) Current–voltage curves under various illumination intensities. c) Photocurrent and responsivity as a function of the incident illumination intensity. d) Dependence of detectivity on the light intensity. e) The reproducible on/off switching with the chopped frequency of 0.2 Hz (16.0 mW mm^{-2}). f) A high-resolution photoresponse of the photodetector to indicate the rise and decay time constants. Comparison of infrared photodetection performance of the single $GaAs_xSb_{1-x}$ nanowire devices under the illumination intensity of 0.35 mW mm^{-2} (1550 nm laser). g) Dark current, h) responsivity, and i) detectivity as a function of the As concentration. The source–drain bias is 2 V and gate bias is 0 V.

in the literature (**Table 1**), designating the rapid generation and recombination process of the electron–hole pairs occurred in the NWs when illuminated by the light. This extraordinary photodetection performance with high R and D^* values, as well as the fast response speed, could be attributed to the relatively high mobility, superior crystal quality, and few surface states of the NWs, etc.

Since the highly-crystalline $GaAs_xSb_{1-x}$ NWs with different chemical stoichiometries have been readily achieved by the thiourea-assisted CVD process, it is also important to explore the relationship between the NW composition and the fabricated NW photodetector properties. The photodetection performance of other representative $GaAs_xSb_{1-x}$ NW devices are displayed in Figures S13–S17 (Supporting Information). The variation of dark current, responsivity and detectivity of the NW photodetectors with different composition are systematically investigated under the illumination intensity of 0.35 mW mm^{-2} in Figure 6g–i and compiled in **Table 2**. It can be seen that there is a significant difference among their performances. Explicitly, the dark current of NW devices drops dramatically with the increasing As composition of NW channels. The reduced dark current corresponds to the less free hole carrier concentration in the NW channel, which results from the fewer amount of Sb-related point defects with more As concentration incorporated in the NWs. This observation is in accordance with the FET properties that the higher I_{ON}–I_{OFF} ratio and the reduced threshold voltage are yielded due to the replacement of Sb atoms with As atoms. As the As composition rises, the responsivity of $GaAs_xSb_{1-x}$ NW devices is found to experience a moderate downward trend. Typically, the device photocurrent is proportional to the carrier mobility and carrier lifetime of the devices (i.e., $I_{ph} \propto \mu\tau$).[39] On the one hand, as shown in Figure 5d, the NW device's carrier mobility decreases with the increasing As content, which would result in the decreasing photocurrent. Similarly, with the increasing Sb content, the hole concentration of $GaAs_xSb_{1-x}$ NWs would

Table 1. Performance comparison of single NW NIR photodetectors.

Channel material	Incident wavelength	Source–drain bias	Responsivity [A W^{-1}]	Detectivity [Jones]	Rise/decay time	Ref.
InGaAs	1550 nm@RT	0.5 V	7.3×10^3	4.2×10^{10}	480/810 µs	[3b]
InGaAs	1600 nm@RT	0.5 V	6.5×10^3	–	70/280 ms	[30]
InGaAs	1550 nm@77 K	1 V	5.75	–	–	[31]
InAsP	1700 nm@RT	0.5 V	5417	–	–	[32]
GaAsSb	1550 nm@RT	0.15	1.44	6.55×10^8	–	[33]
GaAsSb	1310 nm@RT	1 V	1.7×10^3	–	60/250 ms	[34]
GaSb/GaInSb	1550 nm@RT	1 V	1.05×10^3	–	2/3.7 ms	[35]
InGaSb	1550 nm@RT	2 V	6×10^3	3.7×10^9	38/53 µs	[3c]
Graphene/InAs	1000 nm@RT	2 V	≈0.5	–	–	[36]
InAs	632–1470 nm@RT	2 V	5.3×10^3	–	–	[37]
GaAsSb/InP	1300 nm@RT	1.5 V	325.1	4.7×10^{10}	–	[38]
GaAsSb	1550 nm@RT	2 V	5.4×10^4	2.5×10^{10}	80/104 µs	this work

increase accordingly (Figure S18, Supporting Information), which lead to the increase of surface recombination velocity.[3e,40] Due to a certain amount of surface states, this high surface recombination velocity would give the high non-radiative recombination rate, degrading the internal quantum efficiency of $GaAs_xSb_{1-x}$ NWs with the higher Sb content.[41] This could also be reflected by the slightly enhanced response speed of ternary $GaAs_xSb_{1-x}$ NW photodetector as compared with that of the GaSb NW device (Table 2). Eventually, the high Sb concentration would adversely affect the carrier lifetime of $GaAs_xSb_{1-x}$ NW photodetector. In this case, it is anticipated that the photoresponse of those NWs would not witness a sharp fall with the increasing As content, although their carrier mobilities are obviously different. Technically, the detectivity of $GaAs_xSb_{1-x}$ NW photodetectors is impacted by the integrated effect of responsivity and dark current. It can be seen that the detectivity rises gradually, reaching a peak at $x = 0.18$, then it continues to decline with the increasing As content later. Evidently, the dramatic decrease of dark current with the higher As content contributes to the enhancement of device detectivity. Similar to the FET results, the characteristic parameters of photodetection would also interplay with each other. Thus, the ideal photodetector performance can be attained by finely adjusting the composition of $GaAs_xSb_{1-x}$ NWs. Anyway, the excellent photodetection performance of $GaAs_xSb_{1-x}$ NW devices demonstrates clearly the robustness of the thiourea-assisted CVD method developed in this work. Additional future works can be focused on the implementation of *p*–*n* junctions, metal-semiconductor Schottky junctions and heterostructures to further refrain the detectivity degradation in the near-infrared waveband.

3. Conclusions

In conclusion, the Sb-rich $GaAs_xSb_{1-x}$ nanowires with tunable stoichiometry have been successfully fabricated by the thiourea-assisted CVD. The crystal structures, electronic and optoelectronic properties of obtained nanowires were carefully characterized. Due to the formation of Sb—S bonding on the nanowire surface, large aspect-ratio $GaAs_xSb_{1-x}$ nanowires can be readily grown on amorphous substrates with high yield and excellent morphological homogeneity. As compared with the GaSb NWs grown without thiourea, it is evident that the nanowire device properties can be substantially enhanced after utilizing thiourea passivation. More importantly, the As content is revealed to have a significant effect on the device performance of $GaAs_xSb_{1-x}$ nanowires. Introducing the As composition into the nanowires would decrease their carrier concentration and mobility while favor lowering the devices' off-state current. When operated as near-infrared photodetectors, the dark current can be dramatically reduced without sacrificing much on the responsivity by controlling the As content. This outstanding device performance, including the fast near-infrared photoresponse in tens

Table 2. Comparison of the photodetection performance among different $GaAs_xSb_{1-x}$ NW devices under the illumination intensity of 0.35 mW mm^{-2}. The average data of each characteristic parameter are compiled in this table.

$GaAs_xSb_{1-x}$ Photodetector	Responsivity [A W^{-1}]	Detectivity [Jones]	EQE [%]	Rise Time [µs]	Decay Time [µs]
GaSb	12 013	2.51×10^9	9.63×10^5	116	145
$GaAs_{0.05}Sb_{0.95}$	11 714	2.58×10^9	9.38×10^5	95	136
$GaAs_{0.11}Sb_{0.89}$	10 027	2.86×10^9	8.04×10^5	96	126
$GaAs_{0.18}Sb_{0.82}$	8042	3.38×10^9	6.45×10^5	82	115
$GaAs_{0.25}Sb_{0.75}$	2995	1.57×10^9	2.40×10^5	74	97
$GaAs_{0.34}Sb_{0.66}$	910	6.84×10^8	7.30×10^4	92	114

of microseconds, suggests the promising potency of $GaAs_xSb_{1-x}$ NWs for advanced electronic and optoelectronic devices.

4. Experimental Section

Synthesis of $GaAs_xSb_{1-x}$ nanowires: The synthesis of $GaAs_xSb_{1-x}$ nanowires was processed by a solid-source CVD method in a dual-zone horizontal tube furnace, including the upstream and downstream zones. At first, the Au catalyst films (≈0.5 nm) were predeposited onto Si/SiO_2 substrates (50 nm thick thermally grown oxide) by thermal evaporation under a vacuum of less than 5×10^{-6} Torr. In order to obtain different chemical stoichiometries of $GaAs_xSb_{1-x}$ nanowires, GaSb (99.999% purity), and GaAs (99.999% purity) were mixed with different mass ratios (i.e., 20:1, 2:1, 1:1, 1:1.5 and 1:2 in wt%) as the solid source. Then, the well-mixed GaAs/GaSb powders held within a boron nitride crucible were placed in the center of the quartz tube of the upstream zone. The thiourea placed in an Al_2O_3 crucible and the Si/SiO_2 substrates with predeposited Au films are positioned in the middle of the two zones and the center of the quartz tube of the downstream zone, respectively. After pumping down the system to 2×10^{-3} Torr, the high-purity H_2 as a carrier gas with a flow rate of 100 sccm is brought into the CVD system and the pressure of the chamber is maintained at 1.8 Torr. Next, the growth temperature at upstream and downstream zones were carefully adjusted to obtain the high-quality NWs with different chemical stoichiometries. With regard to the weight ratio of 20:1, for example, both upstream and downstream zones were heated to 730 and 600 °C in 8 min, respectively, which were subsequently kept for a duration of 12 min. The location of the thiourea-containing crucible was controlled to have a temperature of 500 °C. After the growth, the system is cooled to the ambient temperature under the H_2 gas atmosphere. The detailed growth parameters for all the components are listed in Table S1 (Supporting Information).

Materials Characterization: The surface morphologies of synthesized $GaAs_xSb_{1-x}$ NWs were characterized by a scanning electron microscope (XL30, FEI/Philips ESEM-FEG) and a transmission electron microscope (CM20, Philips). The corresponding crystal structures are examined by analyzing the X-ray diffraction pattern and imaging with high-resolution TEM (Tecnai G^2 F30, FEI). The elemental compositions were determined by the EDS attached to the Philips CM20 and Tecnai F30 and also an EELS attached to the JEM-200F. For TEM imaging, the NWs were first suspended in anhydrous ethanol solution through ultrasonication and transferred onto the grid by drop-casting. Also, the surface elemental analysis was carried out by X-ray photoelectron spectroscopy (model 5802, ULVAC-PHI).

Device Fabrication and Measurement: The $GaAs_xSb_{1-x}$ NW FETs were fabricated by drop-casting the NW suspension onto degenerately boron-doped *p-type* Si substrates with a 50 nm thick thermally grown gate oxide. The source and drain regions with a 2 µm channel length are first defined by utilizing photolithography, followed by the electron-beam deposition of 60 nm thick Ni electrodes and lift-off process. The electronic and optoelectronic performance of the fabricated back-gated NW FETs were measured with a standard electrical probe station and an Agilent 4155C semiconductor analyzer. For the photodetector characterization, the 1550 nm laser was used as the light source, whose power was calibrated and measured by a power meter (PM400, Thorlabs). The irradiation power was tuned by a modulator (AFG 2005, Good Will) connecting to the 1550 nm laser source. High-resolution time response curves of the photodetector were recorded by a digital oscilloscope (TBS 1102B-EDU, Tektronix) combined with a low-noise current preamplifier (SR570, Stanford Research Systems).

Supporting Information

Supporting Information is available from the Wiley Online Library or from the author.

Acknowledgements

W.W. and S.P.Y. contributed equally to this work. This research was financially supported by the Research Fellow Scheme (No. RFS2021-1S04) and the Theme-based Research (No. T42-103/16-N) of the Research Grants Council of Hong Kong SAR, China, and Foshan Innovative and Entrepreneurial Research Team Program (No. 2018IT100031).

Conflict of Interest

The authors declare no conflict of interest.

Data Availability Statement

The data that support the findings of this study are available from the corresponding author upon reasonable request.

Keywords

GaAsSb, nanowires, near-infrared, photodetectors, surface passivation, thiourea

Received: June 24, 2021
Revised: August 10, 2021
Published online: September 23, 2021

[1] a) R. X. Yan, D. Gargas, P. D. Yang, *Nat. Photonics* **2009**, *3*, 569; b) J. A. del Alamo, *Nature* **2011**, *479*, 317; c) H. Riel, L. E. Wernersson, M. W. Hong, J. A. del Alamo, *MRS Bull.* **2014**, *39*, 668; d) J. F. Wang, M. S. Gudiksen, X. F. Duan, Y. Cui, C. M. Lieber, *Science* **2001**, *293*, 1455; e) L. F. Shen, E. Y. B. Pun, J. C. Ho, *Mater. Chem. Front.* **2017**, *1*, 630; f) R. R. LaPierre, M. Robson, K. M. Azizur-Rahman, P. Kuyanov, *J. Phys. D: Appl. Phys.* **2017**, *50*, 123001.

[2] a) J. Wallentin, N. Anttu, D. Asoli, M. Huffman, I. Aberg, M. H. Magnusson, G. Siefer, P. Fuss-Kailuweit, F. Dimroth, B. Witzigmann, H. Q. Xu, L. Samuelson, K. Deppert, M. T. Borgstrom, *Science* **2013**, *339*, 1057; b) X. Z. Wang, D. Pan, Y. X. Han, M. Sun, J. H. Zhao, Q. Chen, *ACS Appl. Mater. Interfaces* **2019**, *11*, 38973; c) H. D. Li, H. Alradhi, Z. M. Jin, E. A. Anyebe, A. M. Sanchez, W. M. Linhart, R. Kudrawiec, H. H. Fang, Z. M. Wang, W. D. Hu, Q. D. Zhuang, *Adv. Funct. Mater.* **2018**, *28*, 1705382.

[3] a) J. J. Hou, F. Y. Wang, N. Han, F. Xiu, S. P. Yip, M. Fang, H. Lin, T. F. Hung, J. C. Ho, *ACS Nano* **2012**, *6*, 9320; b) H. Zhang, W. Wang, S. Yip, D. P. Li, F. Z. Li, C. Y. Lan, F. Wang, C. T. Liu, J. C. Ho, *J. Mater. Chem. C* **2020**, *8*, 17025; c) D. P. Li, C. Y. Lan, A. Manikandan, S. Yip, Z. Y. Zhou, X. G. Liang, L. Shu, Y. L. Chueh, N. Han, J. C. Ho, *Nat. Commun.* **2019**, *10*, 1664; d) S. Yip, D. P. Li, F. Z. Li, W. Wang, X. L. Kang, Y. Meng, H. Zhang, Z. X. Lai, F. Wang, J. C. Ho, *J. Mater. Chem. C* **2020**, *8*, 13189; e) L. X. Li, D. Pan, Y. Z. Xue, X. L. Wang, M. L. Lin, D. Su, Q. L. Zhang, X. Z. Yu, H. So, D. H. Wei, B. Q. Sun, P. H. Tan, A. L. Pan, J. H. Zhao, *Nano Lett.* **2017**, *17*, 622.

[4] a) J. Huh, H. Yun, D. C. Kim, A. M. Munshi, D. L. Dheeraj, H. Kauko, A. T. J. van Helvoort, S. Lee, B. O. Fimland, H. Weman, *Nano Lett.* **2015**, *15*, 3709; b) S. Nalamati, S. Devkota, J. Li, R. Lavelle, B. Huet, D. Snyder, A. Penn, R. Garcia, L. Reynolds, S. Iyer, *ACS Appl. Electron. Mater.* **2020**, *2*, 3109.

[5] X. M. Yuan, P. Caroff, J. Wong-Leung, H. H. Tan, C. Jagadish, *Nanoscale* **2015**, *7*, 4995.

[6] E. Ahmad, M. R. Karim, S. Bin Hafiz, C. L. Reynolds, Y. Liu, S. Iyer, *Sci. Rep.* **2017**, *7*, 10111.
[7] a) D. D. Ren, D. L. Dheeraj, C. J. Jin, J. S. Nilsen, J. Huh, J. F. Reinertsen, A. M. Munshi, A. Gustafsson, A. T. J. van Helvoort, H. Weman, B. O. Fimland, *Nano Lett.* **2016**, *16*, 1201; b) S. Conesa-Boj, D. Kriegner, X. L. Han, S. Plissard, X. Wallart, J. Stangl, A. F. I. Morral, P. Caroff, *Nano Lett.* **2014**, *14*, 326; c) E. Alarcon-Llado, S. Conesa-Boj, X. Wallart, P. Caroff, A. F. I. Morral, *Nanotechnology* **2013**, *24*, 405707.
[8] I. Ferain, C. A. Colinge, J. P. Colinge, *Nature* **2011**, *479*, 310.
[9] H. Potts, M. Friedl, F. Amaduzzi, K. C. Tang, G. Tutuncuoglu, F. Matteini, E. Alarcon Llado, P. C. McIntyre, A. F. I. Morral, *Nano Lett.* **2016**, *16*, 637.
[10] a) Y. N. Guo, T. Burgess, Q. Gao, H. H. Tan, C. Jagadish, J. Zou, *Nano Lett.* **2013**, *13*, 5085; b) Z. X. Yang, F. Y. Wang, N. Han, H. Lin, H. Y. Cheung, M. Fang, S. Yip, T. F. Hung, C. Y. Wong, J. C. Ho, *ACS Appl. Mater. Interfaces* **2013**, *5*, 10946.
[11] a) Z. D. Wang, M. Yoshida, B. George, *Comput. Theor. Chem.* **2013**, *1017*, 91; b) V. P. Timchenko, A. L. Novozhilov, O. A. Slepysheva, *Russ. J. Gen. Chem.* **2004**, *74*, 1046; c) B. P. Singh, V. Singh, R. C. Tyagi, T. P. Sharma, *Appl. Surf. Sci.* **2008**, *254*, 2233.
[12] a) Y. Fukuda, N. Sanada, M. Kuroda, Y. Suzuki, *Appl. Phys. Lett.* **1992**, *61*, 955; b) Y. Fukuda, M. Shimomura, N. Sanada, M. Nagoshi, *J. Appl. Phys.* **1994**, *76*, 3632; c) Y. Fukuda, Y. Suzuki, N. Sanada, M. Shimomura, S. Masuda, *Phys. Rev. B* **1997**, *56*, 1084; d) M. V. Lebedev, E. V. Kunitsyna, W. Calvet, T. Mayer, W. Jaegermann, *J. Phys. Chem. C* **2013**, *117*, 15996.
[13] Z. X. Yang, N. Han, M. Fang, H. Lin, H. Y. Cheung, S. P. Yip, E. J. Wang, T. F. Hung, C. Y. Wong, J. C. Ho, *Nat. Commun.* **2014**, *5*, 5249.
[14] a) S. P. Yip, L. F. Shen, J. C. Ho, *Nanotechnology* **2019**, *30*, 202003; b) B. M. Borg, L. E. Wernersson, *Nanotechnology* **2013**, *24*, 202001.
[15] a) H. Ye, Z. Y. Yu, S. Kodambaka, V. B. Shenoy, *Appl. Phys. Lett.* **2012**, *100*, 263103; b) H. J. Joyce, Q. Gao, H. H. Tan, C. Jagadish, Y. Kim, X. Zhang, Y. N. Guo, J. Zou, *Nano Lett.* **2007**, *7*, 921.
[16] J. Johansson, L. S. Karlsson, C. P. T. Svensson, T. Martensson, B. A. Wacaser, K. Deppert, L. Samuelson, W. Seifert, *Nat. Mater.* **2006**, *5*, 574.
[17] a) Y. C. Choi, S. I. Seok, *Adv. Funct. Mater.* **2015**, *25*, 2892; b) N. Bao, L. Shen, T. Takata, K. Domen, A. Gupta, K. Yanagisawa, C. A. Grimes, *J. Phys. Chem. C* **2007**, *111*, 17527.
[18] L. F. Zhao, Z. Tan, R. X. Bai, N. Cui, J. Wang, J. Xu, *Appl. Phys. Express* **2013**, *6*, 056502.
[19] Y. Lechaux, A. B. Fadjie-Djomkam, M. Pastorek, X. Wallart, S. Bollaert, N. Wichmann, *J. Appl. Phys.* **2018**, *124*, 175302.
[20] N. Han, F. Y. Wang, J. J. Hou, S. P. Yip, H. Lin, F. Xiu, M. Fang, Z. X. Yang, X. L. Shi, G. F. Dong, T. F. Hung, J. C. Ho, *Adv. Mater.* **2013**, *25*, 4445.
[21] X. M. Zou, X. Q. Liu, C. L. Wang, Y. Jiang, Y. Wang, X. H. Xiao, J. C. Ho, J. C. Li, C. Z. Jiang, Q. H. Xiong, L. Liao, *ACS Nano* **2013**, *7*, 804.
[22] a) C. Thelander, C. Rehnstedt, L. E. Froberg, E. Lind, T. Martensson, P. Caroff, T. Lowgren, B. J. Ohlsson, L. Samuelson, L. E. Wernersson, *IEEE Trans. Electron Dev.* **2008**, *55*, 3030; b) N. Singh, A. Agarwal, L. K. Bera, T. Y. Liow, R. Yang, S. C. Rustagi, C. H. Tung, R. Kumar, G. Q. Lo, N. Balasubramanian, D. L. Kwong, *IEEE Electr. Device Lett.* **2006**, *27*, 383; c) J. Appenzeller, J. Knoch, M. I. Bjork, H. Riel, H. Schmid, W. Riess, *IEEE Trans. Electron Dev.* **2008**, *55*, 2827.
[23] K. A. Dick, J. Bolinsson, B. M. Borg, J. Johansson, *Nano Lett.* **2012**, *12*, 3200.
[24] a) M. Hakala, M. J. Puska, R. M. Nieminen, *J. Appl. Phys.* **2002**, *91*, 4988; b) T. Higashino, Y. Kawamura, M. Fujimoto, A. Kondo, H. Takasaki, N. Inoue, *Jpn. J. Appl. Phys.* **2002**, *41*, 1012.
[25] Y. Y. Peter, M. Cardona, *Fundamentals of Semiconductors: Physics and Materials Properties*, Springer, Berlin **2005**.
[26] a) L. M. Herz, *ACS Energy Lett.* **2017**, *2*, 1539; b) M. Z. Huang, W. Y. Ching, *J. Phys. Chem. Solids* **1985**, *46*, 977.
[27] M. Levinshtein, S. Rumyantsev, M. Shur, *Handbook Series on Semiconductor Parameters*, World Scientific, Singapore **1996**.
[28] a) C. Y. Lan, Z. Y. Zhou, Z. F. Zhou, C. Li, L. Shu, L. F. Shen, D. P. Li, R. T. Dong, S. P. Yip, J. Ho, *Nano Res.* **2018**, *11*, 3371; b) C. Y. Lan, C. Li, Y. Yin, H. Y. Guo, S. Wang, *J. Mater. Chem. C* **2015**, *3*, 8074.
[29] X. Liu, L. L. Gu, Q. P. Zhang, J. Y. Wu, Y. Z. Long, Z. Y. Fan, *Nat. Commun.* **2014**, *5*, 4007.
[30] H. Tan, C. Fan, L. Ma, X. H. Zhang, P. Fan, Y. K. Yang, W. Hu, H. Zhou, X. J. Zhuang, X. L. Zhu, A. L. Pan, *Nano-Micro Lett.* **2016**, *8*, 29.
[31] C. Zhou, X. T. Zhang, K. Zheng, P. P. Chen, W. Lu, J. Zou, *Nano Lett.* **2017**, *17*, 7824.
[32] P. Y. Ren, W. Hu, Q. L. Zhang, X. L. Zhu, X. J. Zhuang, L. Ma, X. P. Fan, H. Zhou, L. Liao, X. F. Duan, A. L. Pan, *Adv. Mater.* **2014**, *26*, 7444.
[33] Z. Y. Li, X. M. Yuan, L. Fu, K. Peng, F. Wang, X. Fu, P. Caroff, T. P. White, H. H. Tan, C. Jagadish, *Nanotechnology* **2015**, *26*, 445202.
[34] L. Ma, X. H. Zhang, H. L. Li, H. Tan, Y. K. Yang, Y. D. Xu, W. Hu, X. L. Zhu, X. J. Zhuang, A. L. Pan, *Semicond. Sci. Technol.* **2015**, *30*, 105033.
[35] L. Ma, W. Hu, Q. L. Zhang, P. Y. Ren, X. J. Zhuang, H. Zhou, J. Y. Xu, H. L. Li, Z. P. Shan, X. X. Wang, L. Liao, H. Q. Xu, A. L. Pan, *Nano Lett.* **2014**, *14*, 694.
[36] J. S. Miao, W. D. Hu, N. Guo, Z. Y. Lu, X. Q. Liu, L. Liao, P. P. Chen, T. Jiang, S. W. Wu, J. C. Ho, L. Wang, X. S. Chen, W. Lu, *Small* **2015**, *11*, 936.
[37] J. S. Miao, W. D. Hu, N. Guo, Z. Y. Lu, X. M. Zou, L. Liao, S. X. Shi, P. P. Chen, Z. Y. Fan, J. C. Ho, T. X. Li, X. S. Chen, W. Lu, *ACS Nano* **2014**, *8*, 3628.
[38] Z. Y. Li, X. M. Yuan, Q. Gao, I. Yang, L. Li, P. Caroff, M. Allen, J. Allen, H. H. Tan, C. Jagadish, L. Fu, *Nanotechnology* **2020**, *31*, 244002.
[39] A. Rose, *Concepts in Photoconductivity and Allied Problems*, Robert E. Krieger Publishing Co, New York **1978**.
[40] L. Jastrzebski, J. Lagowski, H. C. Gatos, *Appl. Phys. Lett.* **1975**, *27*, 537.
[41] J. Treu, T. Stettner, M. Watzinger, S. Morkotter, M. Doblinger, S. Matich, K. Saller, M. Bichler, G. Abstreiter, J. J. Finley, J. Stangl, G. Kobmuller, *Nano Lett.* **2015**, *15*, 3533.